Journal Name

ARTICLE TYPE

Cite this: DOI: 00.0000/xxxxxxxxxx

The self out-of-plane oriented $La_2O_2CO_3$ film: an integration tool for fiber textured ferroelectric thin films

Ewout Picavet,*[a] Hannes Rijckaert,[a] Eduardo Solano,[b] Oier Bikondoa,[c] Edgar Gutierrez Fernandez,[c] Petriina Paturi,[d] Laura Van Bossele,[a] Henk Vrielinck,[e] Jeroen Beeckman,[f] and Klaartje De Buysser [a]

Received Date
Accepted Date

DOI: 00.0000/xxxxxxxxxx

A crucial role in the miniaturization of electronic and photonic components is played by the integration of ferroelectric thin films on silicon (Si) or silicon nitride (SiN) based platforms. Since the properties of ferroelectric thin films strongly depend on their texture quality and crystallographic orientation, the integration of thin films on these platforms is far from trivial. Consequently, this leads to slow, complex and expensive integration processes. To bridge this gap, a high-throughput method for the integration of highly textured ferroelectric thin films on Si or SiN-based platforms is needed. Therefore, we have investigated a method to facilitate the integration of fiber textured ferroelectric thin films by using an ultrathin (∼7 nm) self out-of-plane oriented $La_2O_2CO_3$ template film. In this paper, we report a local deposition route of the $La_2O_2CO_3$ thin film by the scalable inkjet printing method, its inherent out-of-plane crystal orientation, and its lattice match with various ferroelectric thin films. The use of the $La_2O_2CO_3$ template film as an integration tool for ($Pb(Zr,Ti)O_3$, $BaTiO_3$, and $BiFeO_3$) thin films eventually results in strongly fiber-textured ferroelectric stacks, regardless of substrate type. Consequently, the $La_2O_2CO_3$ thin film has the potential to serve as a high-throughput integration tool for fiber textured ferroelectric thin films on Si or SiN-based platforms. Moreover, this integration tool could pave the way for large-scale miniaturization of photonic or electronic devices such as phase modulators, resonators, capacitors, etc.

1 Introduction

High-quality ferroelectric thin films have the potential to pave the way for miniaturization of electronic and photonic devices due to their nanoscale thickness, versatile functionalities, and wide applicability[1–3]. For this reason, various ferroelectric thin films such as HfO_2, $LiNbO_3$, $Pb(Zr,Ti)O_3$, $BaTiO_3$, $BiFeO_3$, and $(Ba,Sr)(Zr,Ti)O_3$ have already been integrated on silicon (Si) or silicon nitride (SiN) platforms to build thin film capacitors[4], piezoelectric actuators[5], and electro-optic modulators[6]. Despite their excellent performance, the integration of thin films is far from trivial, as the inherent anisotropy of ferroelectric materials requires high-quality textured thin films. Consequently, current integration methods for ferroelectric films can typically be divided into two distinct integration pathways. One is the *ex situ* preparation of high quality textured films by methods such as molecular beam epitaxy (MBE), pulsed laser deposition (PLD), and chemical solution deposition (CSD), after which subsequent integration by complex processes such as wafer bonding approaches is required[7–9]. In this way, the high processing temperatures are applied externally, eliminating the risk of damage to the underlying Si-based platform. However, despite the high quality achieved, their applicability for large-scale, high-throughput processing is hindered by the subsequent need for very complex integration methods. Alternatively, textured ferroelectric thin films can be formed *in situ* using template films such as $SrTiO_3$, SiO_2 or metal-based thin films[10–12]. Although *in situ* film formation limits the complexity of integration compared to its *ex situ* counterpart, ferroelectric films formed *in situ* often perform less well. This can be attributed to incompatibility issues related to the template film such as film thickness, optical absorption, or the required (high) thermal processing conditions of the

[a] SCRiPTS, Dept. of Chemistry, Ghent University, Krijgslaan 281-S3, 9000, Ghent, Belgium
[b] NCD-SWEET beamline, ALBA Synchrotron Light Source, Carrer de la Llum 2-26, 08290 Cerdanyola del Vallès, Spain
[c] Dept. of Physics, University of Warwick, Gibbet Hill Road, Coventry CV4 7AL, United Kingdom
[d] Dept. of Physics and Astronomy, University of Turku, Wihuri Physical Laboratory, Vesilinnantie 5, 20014, Turku, Finland
[e] Dept. of Solid State Sciences, Ghent University, Krijgslaan 281-S1, 9000, Ghent, Belgium
[f] LCP group, Dept. of Electronics and Information Systems, Ghent University, Technologiepark - Zwijnaarde 126, 9052, Gent, Belgium

† Electronic Supplementary Information (ESI) available: See DOI: 00.0000/00000000.

ferroelectric films, which can lead to diffusion phenomena [13,14].

Nevertheless, promising results have been obtained recently by introducing a lanthanide (La)-based thin template film deposited by CSD route to integrate ferroelectric $Pb(Zr,Ti)O_3$ thin films for both electronic and photonic applications [15–20]. Unlike other template films, this La-based film has several advantages. First, the thickness of the La-based film can be limited to 5-15 nm instead of using thick intermediate films that severely limit the performance in electro-optical devices. Second, the La-based film is compatible with both electronic and photonic components due to its low optical absorption. Third, this film can be fabricated at relatively low temperatures (475 °C) by wet chemical processes, which is scalable and faster compared to vacuum deposition methods. Fourth, the template film is compatible with various substrates. This enables *in situ* processing routes (f.e. front-end-of-line) on a Si-based platform that can withstand the higher annealing temperatures required to integrate the ferroelectric layer. Alternatively, the film can also serve as an alternative template film in *ex situ* processing routes when *in situ* processing is not an option due to the thermal budget of the processed Si-based platform. In this way, integration flexibility and/or compatibility with the thermal budget during the different processing stages of Si-based platform can be achieved. However, realizing the full potential of the La-based template film as a general integration tool for ferroelectric thin films is currently hindered by the lack of a local deposition route on the Si and SiN-based platform and the unknown crystallographic template film properties. Consequently, there is a need for compatibility with a deposition method that allows local integration of the La-based film, determination of the crystal structure and orientation of the template film, and evaluation of its compatibility with various ferroelectric materials. Understanding the inherent template properties of the film can advance its use as a generic integration tool for various high-quality ferroelectric thin films, while local integration by direct deposition of suitable 2D patterns can exclude the need for additional lithographic and etching steps on the platforms. In this work, local deposition was performed using the inkjet printing method, in which the fluid properties of the inks were optimized along with the ink-substrate interactions to achieve reproducible printing and compatibility with different substrates. Then, the La-based film was structurally characterized to investigate its unit cell structure and orientation. Finally, various ferroelectric thin films were integrated on the La-based template film to evaluate its general use as an integration tool for ferroelectric thin films.

The integration of various ferroelectric thin films such as $Pb(Zr,Ti)O_3$, $BaTiO_3$, and $BiFeO_3$ is demonstrated using a self out-of-plane oriented ultrathin (∼7 nm) $La_2O_2CO_3$ template film. The template film is locally deposited by inkjet printing, which requires optimization of the ink formulation and surface tuning of the substrate to achieve uniform and homogeneous coatings. Subsequent appropriate thermal treatment of the wet film leads to the formation of the monoclinic $La_2O_2CO_3$ phase (Type Ia), which exhibits a b-axis fiber texture by self-orienting its unit cell out-of-plane regardless of the substrate type. Moreover, the in-plane monoclinic lattice parameters show high lattice match with various ferroelectric materials. The subsequent integration of ferroelectric thin films leads to a fiber-textured thin film stack (Figure 1). This comprehensive study can initiate the use of the $La_2O_2CO_3$ template film as a generic integration tool for high-quality ferroelectric thin films on various platforms. In this way, this tool has the potential to pave the way for large-scale miniaturization of photonic or electronic devices such as capacitors, resonators, optical phase modulators, etc.

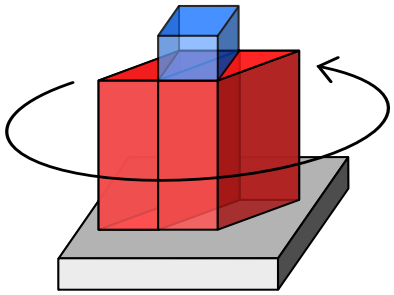

Fig. 1 Illustration of the integration principle using the $La_2O_2CO_3$ template film. The unit cell of the $La_2O_2CO_3$ film (red block) self-orients out-of-plane, while there is no in-plane orientation. Moreover, the $La_2O_2CO_3$ film exhibits a lattice parameter that yields a high lattice match with the unit cell of the ferroelectric film (blue block). Consequently, this ferroelectric stack exhibits a general fiber texture.

2 Experimental

2.1 Ink formulation and characterization

The polyvinylpyrrolidone (PVP) polymer based inks are prepared by dissolving 0.05 g of 40 wt% PVP (Alfa Aesar, 8000 g/mol) solution in H_2O in 10, 20, 40 or 60 mL n-propanol. The intermediate $La_2O_2CO_3$ precursor solution is prepared by dissolving $La(NO_3)_3{\cdot}6H_2O$ (Merck, ≥ 99.99 %) in n-propanol (Merck, ≥ 99.5 %). The molarity of the solution is 0.15 mol L^{-1} for deposition via ink-jet printing yielding a film thickness of 10 nm after annealing. To make the ink suitable for ink-jet printing, the rheological properties of the ink were adjusted by adding ethylene glycol (EG) (Merck, ≥ 99.5 %) to obtain the appropriate jettability. The rheological properties that are measured are the surface tension, viscosity and density of the ink. The surface tension and contact angles are measured with a Krüss GmbH DSA30 instrument, the viscosity with a Brookfield DV-E viscometer (25 °C) and the density is calculated by a threefold weighing measurement of 1 mL ink. The perovskite based inks are prepared based on inks formulations reported in literature: $Pb(Zr,Ti)O_3$ [16], $BaTiO_3$ [21], $BiFeO_3$ [22]. All the inks were filtered with a 0.2 μm filter prior to deposition.

2.2 Chemical solution deposition and thermal treatment

Prior the deposition, the substrates are ultrasonically cleaned with acetone and isopropanol, followed by a heat treatment at 400 °C on a hot plate in order to remove adsorbed organics [23]. Consequently, the PVP polymer film is deposited via means of spin-

coating using a KLM SCC-200 model with a spin rate of 2500 rpm and spin time of 30 s. The deposited PVP polymer film is dried at 200 °C for 10 min on a hotplate before ink-jet printing. The ink was printed using a piezoelectric Dimatix DOD Material Printer DMP-2800 (Dimatix-Fuijifilm inc.) equipped with a Samba cartridge with a 16 μm orifice and 16 nozzles. Homogeneous layers were obtained with the use of 1-16 nozzles, a drop space of 40 μm in x- and y- position, a hotplate temperature of 28 °C, and a print height of 300 μm. A printing waveform with maximum voltages of the waveforms, both jetting and non-jetting, were 33.0 V and 4.29 V, respectively. Together with a jetting frequency of 10 kHz, good jettability is ensured. Afterward, the printed layers were dried at 200 °C for 5 min in order to evaporate the solvent and annealed in a dry static air atmosphere with a heating ramp of 12.5 °C min^{-1} to a final temperature of 475 °C for 20 min. In the case of the ferroelectric thin films, the inks were spin-coated at a spin rate of 3000 rpm for 30 s. Afterwards, they are dried at 200 °C for 10 min and annealed at 550 - 800 °C for 60 min in a tube furnace under a flowing O_2 atmosphere of 1 L min^{-1} in order to obtain the desired crystal orientation on the $La_2O_2CO_3$ film.

2.3 Textural characterization

Texture and phase composition of the $La_2O_2CO_3$ thin films were characterized by means of FTIR, GIWAXS, $\theta-2\theta$ measurements, and phi scans. FTIR measurements in the mid infrared were performed in transmission at normal incidence on layers deposited on FZ silicon substrates, using a Bruker Vertex-80v vacuum spectrometer (1.5 mbar dynamic vacuum, mid infrared Globar source, KBr beam splitter, DLaTGS detector). Spectra were recorded with 5 cm^{-1} resolution, in order to largely suppress the Fabry-Perot interference effect of the Si substrate, and divided by the transmission spectrum of an uncoated substrate. The GIWAXS data was obtained at NCD-SWEET beamline at the ALBA Synchrotron Radiation Facility (Spain). The incident X-ray beam energy was set to 12.4 keV (λ = 0.9998 Å) using a channel cut Si (111) monochromator. An array of Be lenses was employed to collimate the beam, obtaining a beam size at sample position of 50 × 150 μm^2 (V × H). The angle of incidence α_i was screened between 0° and 1° and was finally set at 0.25°, ensuring surface sensitivity and using an exposure time of 10 s. The scattering patterns were recorded using a Rayonix LX255-HS area detector, which consists of a pixel array of 1920×5760 pixels (H×V) with a pixel size of 44.27×44.27 μm^2. The scattering vector |q| was calibrated using Cr_2O_3 as a standard sample, obtaining a sample-to-detector distance of 201.65 mm. The intrinsic 2D GIWAXS pattern is corrected as a function of the components of the scattering vector and was integrated or remapped in polar coordinates. It was reported here after integration, yielding the azimuthal angle in the function of the scattering vector (q). $\theta-2\theta$ measurements were performed on a Bruker D8 Advance diffractometer (Cu-Kα λ = 1.54184 Å) equiped with a LynxEye XE-T Silicon strip line detector. The diffraction was measured between $2\theta = 10°$ and 45° with a step width of 0.02° and step time of 10 s for the $La_2O_2CO_3$ films. The ferroelectric films were measured with an additional Ni filter. Measurement parameters were adjusted to $2\theta = 20°$ - 50° with a step width of 0.02° and step time of 4 s. The in-plane texture of the ferroelectric films was determined with a Panalytical Empyrean x-ray diffractometer with Cu K_α radiation, Bragg-Brentano HD beam conditioning, five axis goniometer and PixCel3D detector. The $La_2O_2CO_3$ (130) measurements were done on the XMaS -BM28, the EPSRC-funded UK-CRG beamline at the European Synchrotron Radiation Facility (France)[24]. A Dectris - Pilatus3 × 300k detector (487 × 619 pixels, pixel size 0.172 × 0.172 mm^2) was used to record scattering patterns of the (130) reflection in an azimuthal range of 168 degrees. At each step, an exposition time of 3 seconds was used to collect the data.

2.4 Microstructural characterization

The surface roughness of the $La_2O_2CO_3$ films and the thickness of the PVP polymer film was determined by atomic force microscopy (AFM) on a Bruker Dimension Edge system operating in tapping mode in the air. The Root Mean Square (RMS) roughness values were calculated on 3 μm × 3 μm micrographs. The thickness of the polymeric layers was estimated by producing a scratch with a sharp needle, recording the thickness profile across the scratch with AFM, and subtracting the height differences. Structural properties and thicknesses of the functional films were characterized with a JEOL FEG SEM JSM-7600F operating at an acceleration voltage of 10 keV. For the TEM measurements, a cross-sectional lamella was cut via the FEI Nova 600 Nanolab Dual Beam FIB-SEM *in situ* lift out procedure with an Omniprobe extraction needle and top cleaning. HRTEM images were taken on a JEOL JEM-2200FS TEM operated at 200 kV and equipped with Cs corrector.

3 Results and discussion

3.1 Jettability and wettability of La-containing inks

The integration of La-containing films via the inkjet printing method is only possible if proper droplet formation (jettability) over time is achieved. For this, stable inks with suitable physical fluid properties must be developed. These properties are well-defined and can be related through the dimensionless Ohnesorge number (Oh). It is defined as:

$$Oh = \frac{\eta}{\sqrt{a\rho\gamma}} = \frac{1}{Z} \quad (1)$$

Where η (Pa·s) is the viscosity, a (m) is the orifice diameter of the nozzle, ρ (kg·m^{-3}) is the density, and γ (J·m^{-2}) is the surface tension of the fluid. For stable droplet formation in a drop-on-demand (DOD) printhead, the inverse of the Ohnesorge number, the Z-number being independent of the droplet velocity, should be in the range of 1 - 14[25]. At low values of Z, viscous forces in the solution prevent droplet formation, while at high values the primary droplet is accompanied by satellite droplets. In addition, the ideal fluid properties of the ink are also affected by the ideal fluid mechanics in the selected ink-jet printing set-up. Therefore, the previously formulated ink for spin-coating in the work of George et al.[16], using a La-nitrate precursor in n-propanol (P) as a solvent, could not be used directly because its viscosity (1.951 mPa s) is too low to achieve stable droplet for-

Table 1 Fluid properties of propanol (P) and ethyleneglycol (EG) determined at 20 °C. The Z-number is calculated for an orifice diameter of 16.5 μm

Inks	ρ [kg·m^{-3}]	η [mPa·s]	γ [mJ·m^{-2}]	boiling point [°C]	Z-number
n-propanol (P)	803.2	1.95	20.9	97	8.53
ethylene glycol (EG)	1111.0	18.38	48.3	197	1.62

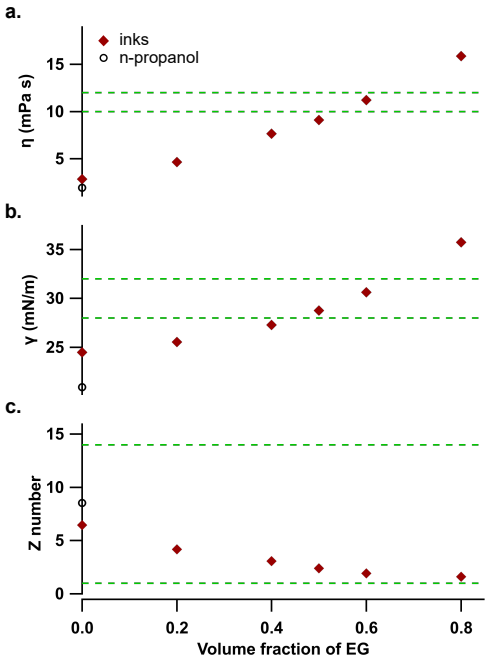

Fig. 2 a. Viscosity, b. Surface tension, c. Z-number of the modified La containing inks as a function of the added volume fraction of EG. Only the fluid properties of a EG volume fraction of 0.6 are all in accordance with the optimal fluid property intervals (horizontal dashed lines) as recommended by the printer manufacturer[26].

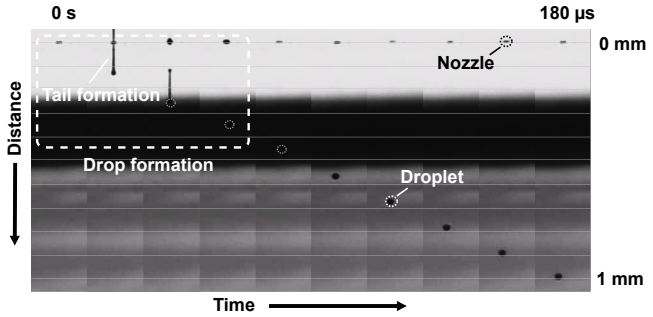

Fig. 3 Drop visualisation using the Dimatix drop watcher. Jetting of spherical droplets from the nozzle in the air. Tail formation is observed, but no satellite droplets are formed. After drop formation, the droplet travels at a speed of 5.55 m/s and remains stationary in flight.

mation during inkjet printing[26]. For this reason, the viscosity of the n-propanol based ink is increased by admixing a more viscous solvent, ethylene glycol (EG, 16.1 mPa s). The physical fluid properties of the respective solvents are collected in Table 1.

The influence on the viscosity (a), the surface tension (b), and Z number (c) of the P-EG inks are present in Figure 2. Compared to the intrinsic properties of P (black circle), the viscosity and surface tension slightly increased upon dissolving the La-nitrate precursor (red square), resulting in a slightly lower Z-number. The EG exhibits a higher density and surface tension compared to P. All fluid properties show an increasing trend with increasing EG/P ratio. The simultaneous strong increase in viscosity with a slight increase in surface tension is reflected in a decrease in Z-number, which is proportional to $\sqrt{\rho}/\eta$ according to equation (1). Although all Z-numbers of the EG/P ratios are in the ideal printing range, the viscosities and surface tension measurements indicate that only a EG volume fraction of 0.6 meets the ideal printing requirements. The actual jetting behaviour of this optimal EG/P ratio can be seen in Figure 3. Here, a tail forms when a droplet is expelled from the nozzle during droplet formation. This tail merges with the droplet after 60 μs to form a single spherical droplet, while no satellite droplets form. Once a spherical droplet is formed, it continues on its path with a vertical traveling speed of 5.55 m/s and remains stationary in flight. It is noteworthy that the ink in the cartridge was jettable for at least 5 months when stored in the closed container, indicating the high stability of the solvent mixture.

In addition to proper jettability, the interaction between the substrate and the droplet upon impact (wettability) plays a critical role in the formation of a homogeneous and uniform coating. Since the print resolution depends on the surface properties, reproducible printing on different Si and SiN-based platforms can only be achieved if there is a similar interaction between ink and substrate. Therefore, the interaction between ink and substrate is tailored by the prior deposition of an amphiphilic polyvinylpyrrolidone (PVP) ($\sim$ 8000 g mol^{-1}) polymer film. By applying the polymer film to the substrate, the surface free energy (SFE, γ_{sv}) of a substrate is modified based on the chemical nature of the polymer, while the surface morphology remains unaffected. In other words, the surface properties depend on the chemical nature of the polymer and are independent of the nature of the substrate[27,28]. In figure 4, this principle is shown by calculating the SFE of a Si substrate before and after coating with PVP. Additionally, a comparison with different PVP-modified substrates (Si, SiO_2, SiN, Indium Tin Oxide (ITO), and glass) is also provided. The two-component (polar and dispersive) Owens-Wendt-Rabel-Kaeble (OWRK) model is used to calculate the SFE based on the contact angles of at least two probe liquids (H_2O and CH_2I_2) with known γ_L, γ_L^D and γ_L^P[29].

Comparing the contact angles of a pristine Si substrate with those of a PVP-treated Si substrate, it is clear that the use of a polymer film is an effective means of altering the ink-substrate interaction, and so to adjust the SFE of a substrate. The chemically amphiphilic nature of the polymer film leads to a preference for both polar and dispersive interactions, resulting in low contact angles of 19.4° with H_2O and 25.3° with CH_2I_2. In particular, the strong decrease in the contact angle with CH_2I_2 after PVP treatment indicates an increased preference for dispersive interac-

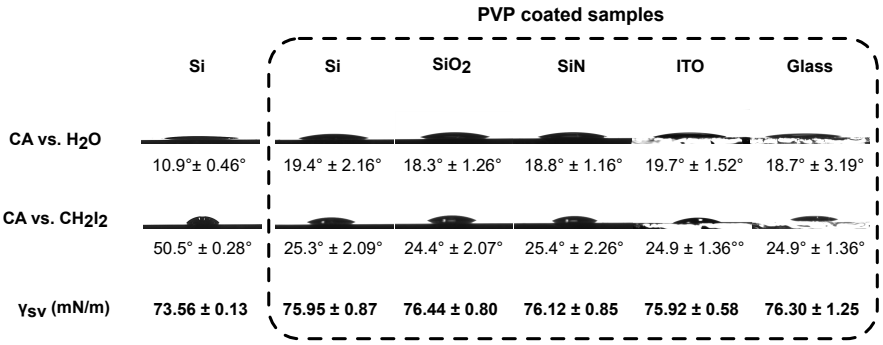

Fig. 4 The ink-substrate interaction can be modified by prior deposition of a PVP polymer film on the substrate, as shown by the different measured contact angles with H_2O and CH_2I_2 of an untreated Si and a PVP-treated Si substrate. Moreover, surface tuning by prior deposition of a PVP polymer leads to a similar SFE, which ensures reproducible ink-substrate interaction, regardless of the substrate type.

tions. This large decrease contributes significantly to the increase in SFE (75.95 mN/m) and ensures adequate wettability with both apolar and polar solvents. The calculation of the contact angles of the different PVP-treated substrates resulted in almost identical values, leading to a similar SFE for the different PVP-treated substrates. This verifies that the surface properties depend on the chemical nature of the polymer and are independent of the substrate. Consequently, setting the SFE by prior PVP film deposition will ensure identical interaction between ink and substrate, resulting in identical print resolution. Additionally, the effect of PVP thickness on surface properties is evaluated, but since similar SFEs are obtained (Figure S1), PVP thickness does not seem to have an impact. For this reason a PVP solution of only 0.0625 wt% is used in this work, as this still ensures reproducible surface modification without the formation of precipitates or inhomogeneous coatings after deposition of the La-containing inks. The thickness of the PVP film could not be accurately determined, as the film thickness for a 0.5 wt% PVP solution is only about 5 nm. Therefore, it is concluded that the PVP film thickness is less than 5 nm.

In addition to ensuring a reproducible ink-substrate interaction, the chemical nature of the PVP polymer exhibits another crucial functionality: complexation of the free La^{3+} ion[28,30,31]. Complexation is required because inks containing free La^{3+} ions tend to make the surface hydrophobic after interaction, which could lead to dewetting phenomena at the surface interface[32,33]. This can be overcome by the presence of amide groups in the PVP polymer, which tend to form complexes due to the interaction between the C=O groups of PVP and the free La^{3+} ion. The general principle of the complexation reaction initiated at the surface interface is shown in Figure 5 (a). By triggering complexation only at the interface, the PVP concentration can be kept very low, which is necessary because PVP cannot otherwise be used as a complexing agent due to precipitation of the La-PVP complex in our ink. The actual effect of PVP complexation at the surface interface on the wetting behaviour is shown in Figure 5 (b, c), where the La-based ink was deposited in a square pattern of 40 $\times$ 40 drops on an untreated SiO_2 (b) and a PVP-treated SiO_2 substrate (c). In the first case, the lack of complexation led to the formation of solvent islands, and no uniform coating was obtained. In contrast, when the substrate was modified by the PVP polymer, the complexation reaction at the interface resulted in a uniform coating with a print resolution of 90 μm. The uniformity of the coating was quantified by surface analysis using atomic force microscopy (AFM) at the centre of the printed film after annealing (Figure 5 (d)) and revealed a very low root mean square roughness (RMS) of 0.176 nm for a 10 nm thick film.

3.2 The self-oriented nature of the $La_2O_2CO_3$ film

After subsequent annealing of the printed film in dry static air at 475 °C, a $La_2O_2CO_3$ film is expected to form according to George et al[16]. The $La_2O_2CO_3$ phase can have three polymorphic structural variants: tetragonal Type I, monoclinic Type Ia, and hexagonal Type II. In Figure 6 (a), the formed $La_2O_2CO_3$ polymorph is determined by comparing the azimuthal integration of the 2D Grazing-Incidence Wide-Angle X-ray Scattering (GIWAXS)

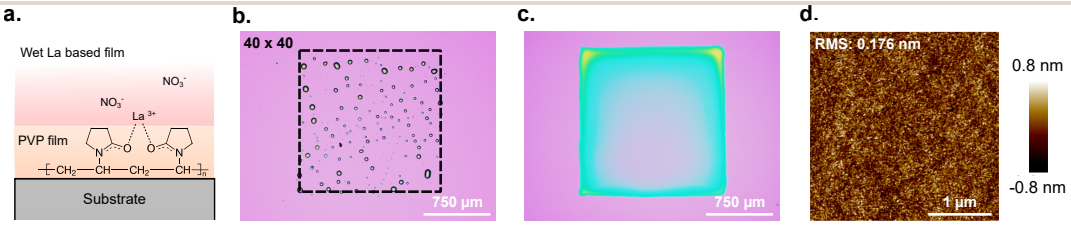

Fig. 5 a. The PVP polymer film induces a complexation reaction at the surface interface. b. A printed square pattern of 40 drops $\times$ 40 drops without prior PVP film deposition shows dewetting phenomena. c. A printed square pattern of 40 drops $\times$ 40 drops with prior PVP film deposition results in adequate ink-substrate interaction d. The inkjet printed $La_2O_2CO_3$ film exhibited very low roughness (RMS of 0.176 nm) for a 10 nm thick film after annealing.

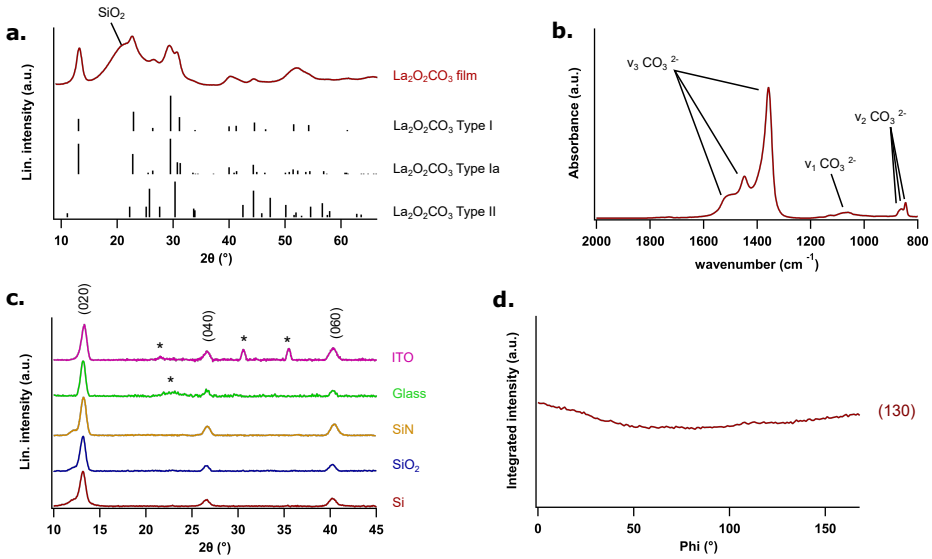

Fig. 6 a. The 1D azimuthally integrated GIWAXS data of the $La_2O_2CO_3$ film is compared with the different $La_2O_2CO_3$ types: tetragonal $La_2O_2CO_3$ Type I (PDF: 00-023-0320), monoclinic Type Ia (PDF: 00-048-1113), and hexagonal Type II (PDF: 00-037-0804). The $La_2O_2CO_3$ film shows a high match with both $La_2O_2CO_3$ Type I and Ia. b. FTIR spectrum of $La_2O_2CO_3$ in the region of the ν_{1-3} bands of CO_3^{-2}. The three-fold splitting of the ν_2 and ν_3 bands is indicative of the monoclinic $La_2O_2CO_3$ Type Ia. c. In the θ - 2θ measurements, only the (0k0) planes are visible, indicating the inherent preferential orientation of the b-axis out-of-plane. The reflections marked with an asterisk are associated with the substrate. d. No in-plane orientation is present because the (130) plane has no in-plane correlation over a ϕ interval of 168°.

recorded images of the film with the different powder diffraction files (PDF) of the $La_2O_2CO_3$ types. The broad additional peak ($2\theta \sim 23°$) can be attributed to the amorphous nature of the SiO_2 substrate and is not related to any crystal plane of the film[34]. The reflections are assigned to the tetragonal Type I phase and/or the monoclinic Type Ia, since they do not show any correspondence with the hexagonal Type II. The reflections could not be assigned to only one of the two types, since Type Ia is the monoclinic distortion of Type I, resulting in a very similar crystal structure and thus an almost identical PDF. However, a distinction between these two $La_2O_2CO_3$ polymorphs can be made by analysing the carbonate species in the film using Fourier Transform Infrared Spectroscopy (FTIR) in the mid IR. In Figure 6 (b), the characteristic CO_3^{-2} bands (ν_1 = 1063 cm^{-1}, ν_2 = 879 cm^{-1} and ν_3 = 1415 cm^{-1}) are indicative of the $La_2O_2CO_3$ phase[35]. As the threefold splitting of the ν_2 and ν_3 modes is assigned to the unique carbonate vibrational mode of the monoclinic $La_2O_2CO_3$ Type Ia phase. The peak splitting itself is attributed to the three nonequivalent carbonate groups in type Ia, since there are only two nonequivalent carbonate groups in Type I. Thus, the FTIR spectrum indicates that the $La_2O_2CO_3$ film exhibits a monoclinic type Ia phase, which according to the work of Hirsch et al.[36], has a space group P21/c (No. 14) with lattice parameters a = 4.076 Å, b = 13.489 Å, c = 5.803 Å, $\alpha = \gamma = 90°$, β = 135.37°. In addition to identifying the $La_2O_2CO_3$ polymorph, the films also exhibit a high degree of texture. In Figure 6 (c), $\theta - 2\theta$ measurements of the $La_2O_2CO_3$ film deposited on different substrates show only diffraction peaks along the [0k0] direction. Consequently, the $La_2O_2CO_3$ film exhibits a preferential out-of-plane b-axis orientation. This preferred orientation is not affected by the type of substrate, since both crystalline (Si and ITO) and amorphous (SiO_2, SiN, and glass) substrates show the same (0k0) planes. In contrast to the preferred out-of-plane orientation, no in-plane orientation was present. In Figure 6 (d), the (130) plane at 2θ = 29.6° and χ = 48° was rotated over a ϕ angular range of 168°. Since the signal intensity is independent of the ϕ angle, no in-plane texture is present. Small variations in signal intensity are related to the integration of the 2D (130) signal at different ϕ angles (Figure S2). In summary, the $La_2O_2CO_3$ film has a self-oriented fiber texture with the b-axis oriented perpendicular to the substrate surface.

Since this phase formation and fiber texture is independent of the nature of the substrate, these must be related to the formation of the $La_2O_2CO_3$ material itself. Phase formation is attributed to the transformation of the $LaONO_3$ intermediate phase during the decomposition of the original $La(NO_3)_3{\cdot}6H_2O$ precursor, due to its sensitivity to gases such as CO_2 and H_2O[37–39]. To evaluate if the PVP polymer acts as the CO_2 and H_2O source, the wet film was annealed with and without the underlying PVP film. As both films yielded self out-of-plane oriented $La_2O_2CO_3$ films, it is concluded that the PVP film only serves as an adhesive and will thermally decompose during the annealing step (Figure S3). Since annealing in ambient air is crucial for the formation of the $La_2O_2CO_3$ phase, it is very likely that phase formation occurs by reaction with CO_2 and H_2O in ambient air via the formation of surface carbonates and hydroxycarbonates[40]. Moreover, also its inherent out-of-plane orientation is attributed to the $La_2O_2CO_3$ material formation. Since all three $La_2O_2CO_3$ polymorphs are assumed to have a layered structure with alternating $La_2O_2^{2+}$ and CO_3^{-2} layers, differing only by local coordination around the La atom or CO_3^{-2} order[35,36,41,42]. In Figure 7 (a), High-Resolution Transmission Electron Microscope (HRTEM) measurements clearly show the presence of the layered structure in the $La_2O_2CO_3$ film, with the $La_2O_2^{2+}$ and CO_3^{-2} layers aligned parallel to the substrate sur-

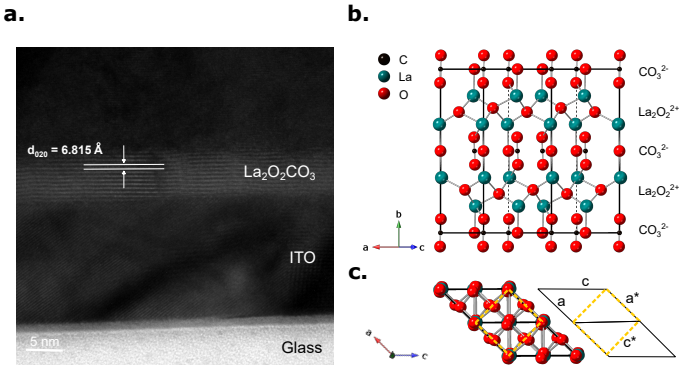

Fig. 7 a. Layered structure visualised by HRTEM on a ITO substrate. b. The alternating $La_2O_2^{2+}$ and CO_3^{-2} layers cause the b-axis out-of-plane orientation of the unit cell. c. The in-plane monoclinic lattice parameter can be converted to a distorted tetragonal lattice. Visualisation of the unit cell was based on the refined data of Hirsch et al.[36]

face. The film thickness is around 7 nm for a concentration of 0.15 mol L^{-1} deposited via inkjet printing (experimental information). The importance of this layered structure for the self-orientation of the unit cell is shown in Figure 7 (b). The layered structure causes the b-axis of the unit cell to be out-of-plane. This concept is supported by the measured interplanar CO_3^{-2} distance value of 6.815 Å in HRTEM, which agrees very well with the (020) planes of the monoclinic Type Ia $La_2O_2CO_3$ phase (d_{020} = 6.745 Å). Consequently, the inherent layered structure of the $La_2O_2CO_3$ phase and its parallel orientation to the surface substrate lead to an out-of-plane orientation of the b-axis. In addition, this gives that the in-plane lattice constants are a = 4.076 Å, c = 5.803 Å, and β = 135.37°[36]. For further lattice mismatch calculations, these monoclinic in-plane lattice parameters will be converted to their distorted tetragonal counterparts based on the strong crystallographic relationship between $La_2O_2CO_3$ Type I (tetragonal) and Ia (monoclinic) mentioned earlier. Figure 7 (c) shows the in-plane relation between the monoclinic (black lines) and distorted tetragonal (dashed yellow) crystal parameters. The monoclinic lattice parameter a (4.076 Å) remains the same, while the longer c parameter (5.803 Å) can be converted to a lattice parameter c* (4.077 Å) via a factor $sin(135.37°)$. Note that the difference between the two parameters is very small, suggesting that the monoclinic parameters can be viewed as a tetragonal distortion (Type Ia) of the original tetragonal unit cell (Type I). For the following lattice mismatch calculations, the lattice parameter a (4.076 Å) is used. It should be noted that this lattice parameter is close to other template materials such as $LaAlO_3$[43] (3.787 Å), $SrTiO_3$[44] (3.905 Å), and MgO[45] (4.216 Å). However, compared to these single crystal substrates, the $La_2O_2CO_3$ film is randomly oriented in-plane.

3.3 The $La_2O_2CO_3$ layer as integration tool

To evaluate the $La_2O_2CO_3$ film as a general integration tool, various ferroelectric thin films were integrated. Based on the approximate in-plane lattice parameter of 4.076 Å, the film exhibits very little mismatch with the ferroelectric films: $Pb(Zr,Ti)O_3$, $BaTiO_3$, $BiFeO_3$. Table 2 lists the lattice parameters of these materials and their respective lattice mismatch with $La_2O_2CO_3$. In all cases, the lattice mismatch was less than 3%, giving a good theoretical lattice match with the various ferroelectric materials.

Table 2 Theoretical lattice mismatch of ferroelectric materials $Pb(Zr,Ti)O_3$[46], $BaTiO_3$[47], $BiFeO_3$[48] with the $La_2O_2CO_3$ film

	lattice parameter 'a'	lattice mismatch
$La_2O_2CO_3$	4.076 Å	-
$BiFeO_3$	3.965 Å	2.713%
$BaTiO_3$	3.999 Å	1.879%
$Pb(Zr,Ti)O_3$	4.055 Å	0.505%

The different ferroelectric thin films (∼ 50 nm) were integrated on the $La_2O_2CO_3$ film using the CSD method (see experimental section). In Figure 8 (a), all ferroelectric films show only strong diffraction peaks along the crystallographic direction [00l]. The small shift of the reflection positions is due to the different unit cell parameters of the ferroelectric materials. Consequently, all the studied films exhibit a preferential out-of-plane orientation when $La_2O_2CO_3$ is used as the template film. Moreover, this induced orientation is also obtained after integrating $Pb(Zr,Ti)O_3$ films on different substrates (Figure S4). This also confirms the inherent self-orientation of the $La_2O_2CO_3$ film and highlights the compatibility of the $La_2O_2CO_3$ film with oxides of other chemical nature such as titanates, zirconates and ferrites. In addition to the out-of-plane texture, no in-plane texture was expected in the functional film because the $La_2O_2CO_3$ film itself also has no in-plane texture. In Figure 8 (b), a pole figure measurement of the (101) plane in the $Pb(Zr,Ti)O_3$ film at 2θ = 31.23° shows two circles at χ values of 45° and 90°. Consequently, the $Pb(Zr,Ti)O_3$ film does not exhibit an in-plane texture, which is consistent with the corresponding fiber texture orientation of the $La_2O_2CO_3$ film. This is partly due to the good lattice match between the $La_2O_2CO_3$ and $Pb(Zr,Ti)O_3$ films and partly due to the lack of a driving force for the in-plane orientation of the $La_2O_2CO_3$ film. Figure 8 (c)

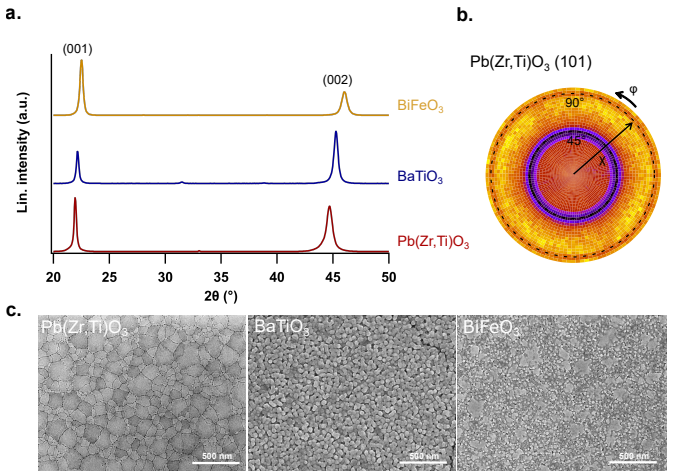

Fig. 8 a. Different ferroelectric materials are integrated on the $La_2O_2CO_3$ film exhibiting out-of-plane texture. b. No in-plane orientation is present as circles are present in the pole figure measurement. c. Dense microstructures with a morphology inherent to the ferroelectric material.

shows planar scanning electron microscopy (SEM) of the respective films deposited on the $La_2O_2CO_3$ films. The surface morphology of the films is dense and smooth, but the microstructure is inherent to the functional material. In summary, the ferroelectric thin films are epitaxially integrated on the $La_2O_2CO_3$ film, but the whole ferroelectric stack has a fiber texture.

4 Conclusion

Compatibility with a local deposition route is achieved by the inkjet printing process. Here, surface tuning through prior deposition of a PVP thin film is critical to achieve reproducible ink-substrate interaction on different substrates and the necessary La-complexation leading to a print resolution of 90 μm. Subsequent annealing of the La-based ink results in monoclinic $La_2O_2CO_3$ thin films (Type Ia) that exhibit out-of-plane self-orientation of the crystallograhpic b-axis caused by the formation of a layered structure of alternating $La_2O_2^{2+}$ and CO_3^{-2} layers. Unlike out-of-plane orientation, the layered structure does not induce an in-plane orientation, resulting in a general fiber texture in the films. Moreover, the in-plane lattice parameter of 4.076 Å yields high theoretical lattice match with various ferroelectric materials. Integration of these materials by wet chemical methods reveals epitaxially integrated films that exhibit the same fiber texture as the $La_2O_2CO_3$ film. This comprehensive study of the $La_2O_2CO_3$ template may initiate its use as an integration tool for various ferroelectric materials requiring texture or as an alternative template film for $SrTiO_3$, MgO, and $LaAlO_3$ since the lattice parameter is quite similar. In addition, various metal oxides such as titanates, zirconates, and ferrites can be integrated. Therefore, the $La_2O_2CO_3$ can be used as a general integration tool for solution-derived ferroelectric thin films. This tool can pave the way for large scale integration of ferroelectric thin films in various applications.

Conflicts of interest

There are no conflicts to declare.

Acknowledgements

The authors thank Davy Deduytsche for performing the X-ray diffraction (XRD) measurements & Kobe De Geest for performing the ellipsometry measurements. GIWAXS experiments were recorded at NCD-SWEET beamline at ALBA synchrotron with collaboration of ALBA staff. TEM measurements were carried out at the UGent TEM Core Facility. Ewout Picavet acknowledges support and funding as an SB-PhD Fellow of the Research Foundation–Flanders (FWO, Grant number 3S041219). Hannes Rijckaert acknowledges support and funding as postdoctoral fellow fundamental research of the Research Foundation–Flanders (FWO, Grant number 1273621N). Petriina Paturi acknowledges the Jenny and Antti Wihuri Foundation for financial support. This work was financially supported by Special Research Fund - UGent (BOF20/GOA/027).

References

1 Z. Shen, C. Y. Tan, K. Yao, L. Zhang and Y. F. Chen, *Sensors and Actuators, A: Physical*, 2016, **241**, 113–119.

2 S. Jeon, *ECS Transactions*, 2020, **98**, 219–223.

3 H. Qiao, C. Wang, W. S. Choi, M. H. Park and Y. Kim, *Materials Science and Engineering R: Reports*, 2021, **145**, 100622.

4 K. Wang, Y. Zhang, S. Wang, Y. Y. Zhao, H. Cheng, Q. Li, X. Zhong and J. Ouyang, *ACS Applied Materials and Interfaces*, 2021, **13**, 22717–22727.

5 P. N. Thao, S. Yoshida and S. Tanaka, *Micromachines*, 2018, **9**, 455.

6 A. N. R. Ahmed, S. Nelan, S. Shi, P. Yao, A. Mercante and D. W. Prather, *Optics Letters*, 2020, **45**, 1112.

7 M. Alexe, S. Senz, A. Pignolet, J. F. Scott, D. Hesse and U. Gösele, *MRS Proceedings*, 1997, **493**, 517.

8 S. Abel, F. Eltes, J. E. Ortmann, A. Messner, P. Castera, T. Wagner, D. Urbonas, A. Rosa, A. M. Gutierrez, D. Tulli, P. Ma, B. Baeuerle, A. Josten, W. Heni, D. Caimi, L. Czornomaz, A. A. Demkov, J. Leuthold, P. Sanchis and J. Fompeyrine, *Nature Materials*, 2019, **18**, 42–47.

9 Y. Yang, T. Liu, L. Bi and L. Deng, *Journal of Alloys and Compounds*, 2021, **860**, 158235.

10 J. Lyu, I. Fina, R. Bachelet, G. Saint-Girons, S. Estandía, J. Gázquez, J. Fontcuberta and F. Sánchez, *Applied Physics Letters*, 2019, **114**, 222901.

11 Y. Lin, B. R. Zhao, H. B. Peng, B. Xu, H. Chen, F. Wu, H. J. Tao, Z. X. Zhao and J. S. Chen, *Applied Physics Letters*, 1998, **73**, 2781–2783.

12 K. Sreenivas, I. Reaney, T. Maeder, N. Setter, C. Jagadish and R. G. Elliman, *Journal of Applied Physics*, 1994, **75**, 232–239.

13 K. Niwa, Y. Kotaka, M. Tomotani, H. Ashida, Y. Goto and S. Otani, *Acta Materialia*, 2000, **48**, 4755–4762.

14 S. Yakovlev, J. Zekonyte, C. H. Solterbeck and M. Es-Souni, *Thin Solid Films*, 2005, **493**, 24–29.

15 J. J. Choi, G. T. Park, C. S. Park, J. W. Lee and H. E. Kim, *Journal of Materials Research*, 2004, **19**, 3671–3678.

16 J. P. George, P. F. Smet, J. Botterman, V. Bliznuk, W. Woestenborghs, D. V. Thourhout, K. Neyts and J. Beeckman, *ACS Applied Materials and Interfaces*, 2015, **7**, 13350–13359.

17 K. Alexander, J. P. George, J. Verbist, K. Neyts, B. Kuyken, D. V. Thourhout and J. Beeckman, *Nature Communications*, 2018, **9**, 1–6.

18 G. F. Feutmba, A. Hermans, J. Puthenparampil George, H. Rijckaert, I. Ansari, D. Van Thourhout and J. Beeckman, *Advanced Optical Materials*, 2021, **9**, 2100149.

19 D. Ban, G. Liu, H. Yu, X. Sun, N. Deng and F. Qiu, *Optical Materials Express*, 2021, **11**, 1733.

20 I. Ansari, J. Puthenparampil George, G. F. Feutmba, T. Van de Veire, A. Pandey, J. Beeckman and D. Van Thourhout, *ACS Photonics*, 2022, **9**, 1944–1953.

21 J. P. George, J. Beeckman, W. Woestenborghs, P. F. Smet, W. Bogaerts and K. Neyts, *Nanoscale research letters*, 2013, **8**, 1–7.

22 B. Yang, L. Jin, R. Wei, X. Tang, L. Hu, P. Tong, J. Yang, W. Song, J. Dai, X. Zhu, Y. Sun, S. Zhang, X. Wang and Z. Cheng, *Small*, 2021, **17**, 1903663.

23 P. Vermeir, F. Deruyck, J. Feys, P. Lommens, J. Schaubroeck

and I. V. Driessche, *Journal of Sol-Gel Science and Technology*, 2012, **62**, 378–388.

24 O. Bikondoa, L. Bouchenoire, S. D. Brown, P. B. Thompson, D. Wermeille, C. A. Lucas, M. Cooper and T. P. Hase, *Philosophical Transactions of the Royal Society A: Mathematical, Physical and Engineering Sciences*, 2019, **377**, 20180237.

25 B. Derby, *Annual Review of Materials Research*, 2010, **40**, 395–414.

26 *Fujifilm Dimatix. Jettable Fluid Formulation Guidelines, http://https://www.fujifilmusa.com/shared/bin/Dimatix-Materials-Printer-Jettable-Fluid-Formulation-Guidelines.pdf*, Accessed: 2023-01-18.

27 T. H. V. Osch, J. Perelaer, A. W. D. Laat and U. S. Schubert, *Advanced Materials*, 2008, **20**, 343–345.

28 A. Matavž, V. Bobnar and B. Malič, *Langmuir*, 2017, **33**, 11893–11900.

29 J. J. Bikerman, *Surface chemistry: theory and applications*, Elsevier, 2013.

30 L. Guo, B. Yan, J. L. Liu, K. Sheng and X. L. Wang, *Dalton Transactions*, 2011, **40**, 632–638.

31 M. Karbowiak, J. Cichos and K. Buczko, *Journal of Physical Chemistry B*, 2014, **118**, 226–239.

32 W. P. Townsend, *Method of rendering a hydrophilic surface hydrophobic*, 1975, US Patent 3,860,447.

33 G. Azimi, R. Dhiman, H. M. Kwon, A. T. Paxson and K. K. Varanasi, *Nature Materials*, 2013, **12**, 315–320.

34 Y. Liang, J. Ouyang, H. Wang, W. Wang, P. Chui and K. Sun, *Applied Surface Science*, 2012, **258**, 3689–3694.

35 R. P. Turcotte, J. O. Sawyer and L. Eyring, *inorganic Chemistry*, 1969, **8**, 238–246.

36 O. Hirsch, K. O. Kvashnina, L. Luo, M. J. Süess, P. Glatzel and D. Koziej, *Proceedings of the National Academy of Sciences of the United States of America*, 2015, **112**, 15803–15808.

37 B. Klingenberg and M. A. Vannice, *Chemistry of materials*, 1996, **8**, 2755–2768.

38 S. Mentus, D. Jelić and V. Grudić, *Journal of Thermal Analysis and Calorimetry*, 2007, **90**, 393 – 397.

39 H. Guerreiro, P. Melnikov, I. Arkhangelsky, L. de Oliveira, G. Wandekoken and V. do Nascimento, *Int. J. Developm. Res.*, 2021, **11**, 43318–43321.

40 S. Bernal, F. Botana, R. García and J. Rodríguez-Izquierdo, *Reactivity of Solids*, 1987, **4**, 23–40.

41 A. Olafsen and H. Fjellvåg, *Journal of Materials Chemistry*, 1999, **9**, 2697–2702.

42 H. Yu, K. Jiang, S. G. Kang, Y. Men and E. W. Shin, *Nanomaterials*, 2020, **10**, 1–13.

43 A. Nakatsuka, O. Ohtaka, H. Arima, N. Nakayama and T. Mizota, *Acta Crystallographica Section E: Structure Reports Online*, 2005, **61**, i148–i150.

44 A. Janotti, B. Jalan, S. Stemmer and C. G. V. D. Walle, *Applied Physics Letters*, 2012, **100**, 262104.

45 Y. Xie, Q. Zhan, T. Shang, H. Yang, B. Wang, J. Tang and R. W. Li, *AIP Advances*, 2017, **7**, 056314.

46 J. F. J. Frantti, J. L. J. Lappalainen, S. E. S. Eriksson, V. L. V. Lantto, S. N. S. Nishio, M. K. M. Kakihana, S. I. S. Ivanov and H. R. H. Rundlöf, *Japanese Journal of Applied Physics*, 2000, **39**, 5697.

47 E. K. Al-Shakarchi and N. B. Mahmood, *Journal of Modern Physics*, 2011, **02**, 1420–1428.

48 B. F. Kubel and H. Schmid, *Neues Jahrb. Mineral. Monatsh*, 1985, **20**, 698–702.